THE BAR PATTERN SPEED OF NGC 1433 ESTIMATED VIA STICKY-PARTICLE SIMULATIONS

P. TREUTHARDT[1], H. SALO[2], P. RAUTIAINEN[2], AND R. BUTA[1]

[1] Department of Physics and Astronomy, University of Alabama, Box 870324, Tuscaloosa, AL 35487, USA
[2] Division of Astronomy, Department of Physical Sciences, University of Oulu, Oulu, FIN-90014, Finland

ABSTRACT

We present detailed numerical simulations of NGC 1433, an intermediate-type barred spiral showing strong morphological features including a secondary bar, nuclear ring, inner ring, outer pseudoring, and two striking, detached spiral arcs known as "plumes." This galaxy is an ideal candidate for recreating the observed morphology through dynamical models and determining the pattern speed. We derived a gravitational potential from an H-band image of the galaxy and simulated the behavior of a two-dimensional disk of 100,000 inelastically colliding gas particles. We find that the closest matching morphology between a B-band image and a simulation occurs with a pattern speed of 0.89 km s^{-1} arcsec^{-1} $\pm$ 5–10%. We also determine that the ratio of corotation radius to the average published bar radius is 1.7 ± 0.3, with the ambiguity in the bar radius being the largest contributor to the error.

Key words: galaxies: individual (NGC 1433) – galaxies: kinematics and dynamics – galaxies: spiral – galaxies: structure

1. INTRODUCTION

NGC 1433 is a well-studied disk galaxy that hosts many interesting morphological features. Detailed studies of the galaxy have been performed by Buta (1986) and, most recently, by Buta et al. (2001). The galaxy is a ringed barred spiral of revised de Vaucouleurs type (R$'_1$)SB(r)ab (Buta et al. 2007; see Figure 1) that displays a nuclear ring or lens as well as inner and outer rings. The nuclear ring is a small, blue feature approximately 19″ in angular diameter that has a small secondary bar crossing it when viewed in the near-infrared (NIR; Buta 1986). The strong primary bar is encircled by a large, knotty, and intrinsically oval inner ring which appears to be formed by four tightly wrapped spiral arm sections that have come together in the bar major and minor axis regions. In the context of passive, non-self-gravitating sticky-particle simulations (Schwarz 1981, 1984), this morphology implies that the inner ring is a 4:1 resonance feature. The faint outer pseudoring is slightly asymmetric and appears relatively smooth compared to the inner ring.

NGC 1433 also harbors two symmetric detached arm segments, or "plumes" (Buta 1984), just outside the leading sections of the inner ring. Like the inner ring, the plumes lie along an ellipse which is oriented parallel to the bar. It is possible that these features are residual traces of a characteristic $m = 4$ spiral pattern that may form in the presence of bars between the inner and outer 4:1 resonances (Rautiainen et al. 2004). Since strong plumes like those seen in NGC 1433 are rarely observed (Buta 1984), it is possible that they are transient features although the simulations of Rautiainen et al. (2004) produced a long-lived four-armed pattern. The plumes, as well as the nucleus and inner ring of the galaxy, are well covered with Hα emission (Figure 1). The outer pseudoring is much fainter and very little Hα emission is seen in the bar region. H I counterparts of the plumes, nuclear ring, inner ring, and outer pseudoring have also been detected (Ryder et al. 1996).

The pattern speed, Ω_p, of a galaxy is an important parameter that governs the overall morphology (Kalnajs 1991). In galaxies with a single perturbation mode, such as a bar or a grand design spiral, Ω_p determines the locations of important resonances. Since NGC 1433 has multiple features that are thought to be

associated with specific resonances, it is an ideal candidate for recreating the observed morphology through dynamical models (e.g., Salo et al. 1999; Rautiainen et al. 2005) and determining Ω_p. This modeling involves determining the gravitational potential from observations and studying the "gas" response on a rigidly rotating nonaxisymmetric component. The gas is modeled as inelastically colliding, or "sticky," particles. Different dynamical parameters are varied until the morphology and kinematics of the numerically simulated galaxy matches, as closely as possible, to the morphology and kinematics of the observed galaxy.

2. ANALYSIS

2.1. Determining the Potential

In order to simulate the dynamics of the galaxy, a gravitational potential must be derived. One way to do this is to assume that the NIR light distribution effectively traces the mass distribution. The potential may then be derived from the convolution of the density with the function $1/R$ (Quillen et al. 1994), combined with an assumption for the vertical density distribution. For NGC 1433, the potential was derived from a 1.65 μm Johnson H-band image obtained in 1996 February with the Cerro Tololo Inter-American Observatory (CTIO) 1.5 m telescope (Buta et al. 2001). B- and I-band images were also taken and the details of these observations are found in Buta et al. (2001). The H-band light distribution is more reliable than B or I for this purpose due to the reduced extinction effects from dust and the weakened influence of young Population I complexes. However, the polar fast Fourier transform (FFT) method we use for the evaluation of gravitational forces (Salo et al. 1999; Laurikainen & Salo 2002) effectively filters out the high-frequency components of the image, and is thus not sensitive to individual SF regions (see Salo et al. 2004). Before the gravitational potential was derived, the H-band image was converted into a surface mass density by assuming a mass-to-light (M/L) ratio accounting for the average disk $B - H$ color gradient using formulae from Bell & de Jong (2001). The seven different M/L models discussed in the Bell & de Jong paper were applied to the H-band image and each corrected image was used to determine a gravitational potential (Figure 2). The M/L models in Bell & de Jong were derived by
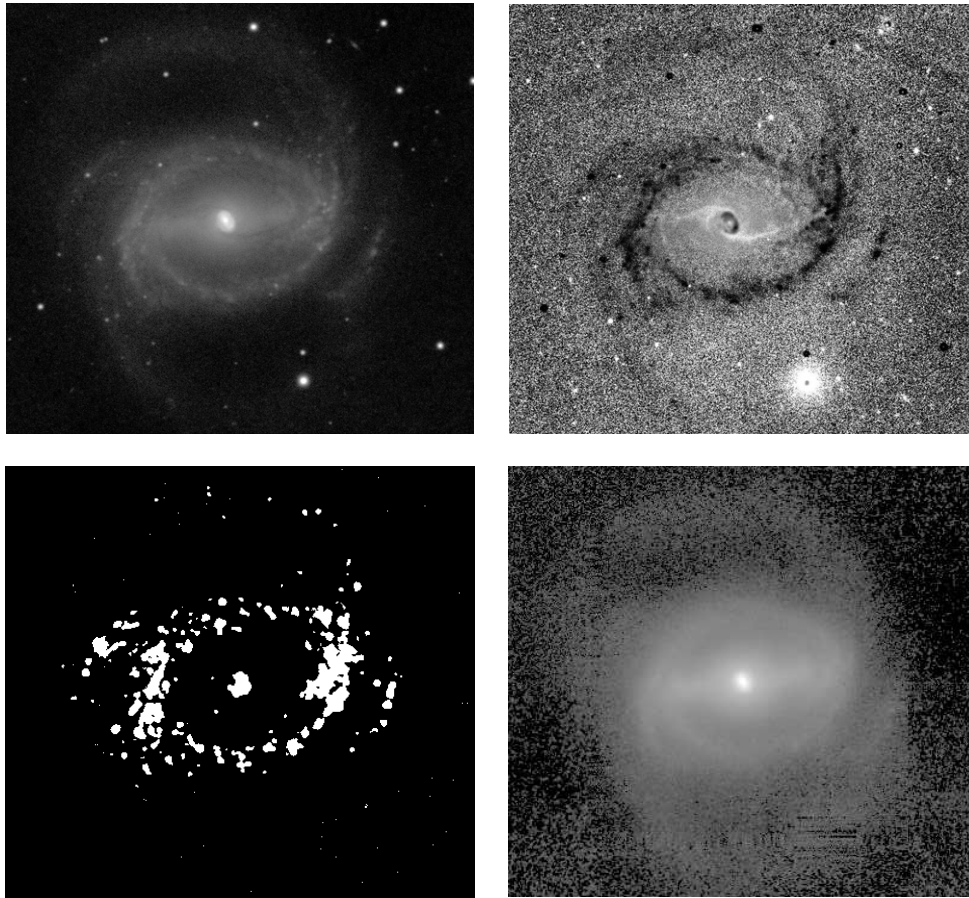
Figure 1. B-band (upper left), $B - I$ color index (upper right), Hα Fabry–Perot (lower left), and H-band (lower right) images displaying the morphology of NGC 1433. In the color index image, the dark areas represent bluer regions, while the white areas represent redder regions. All images are $7.4' \times 6.8'$. The B and $B - I$ images are taken from Buta et al. (2007) while the Hα and H-band images are taken from Buta et al. (2001).
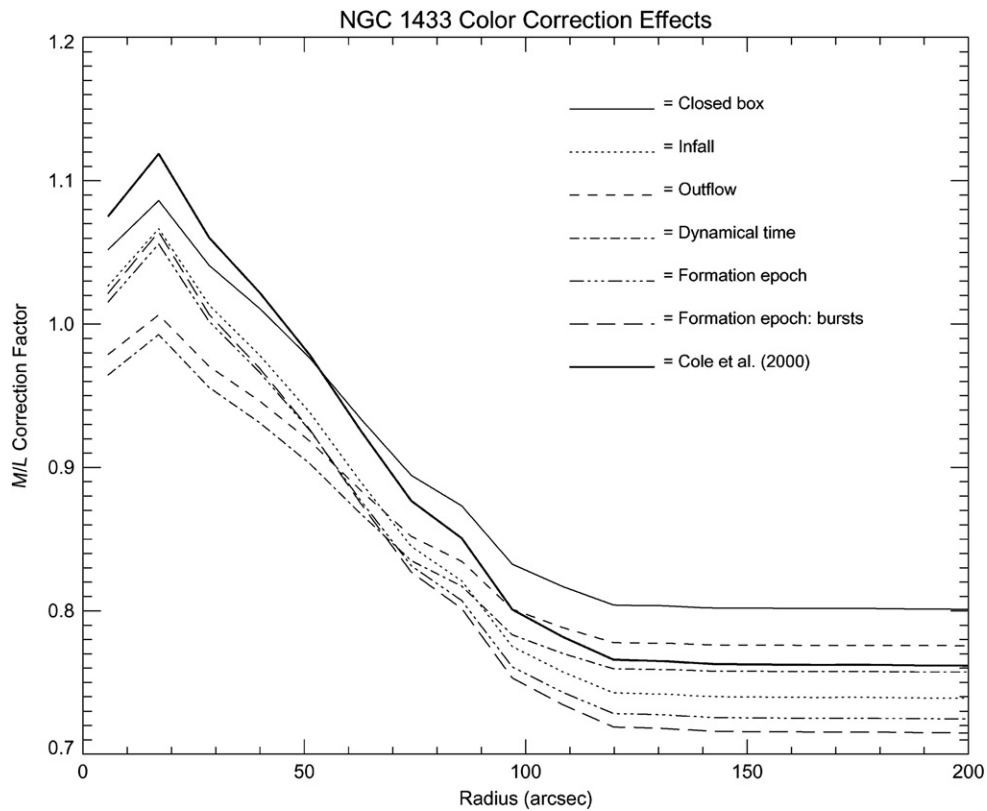

Figure 2. Plot of the radial M/L profiles derived from each of the seven models described in Bell & de Jong (2001).
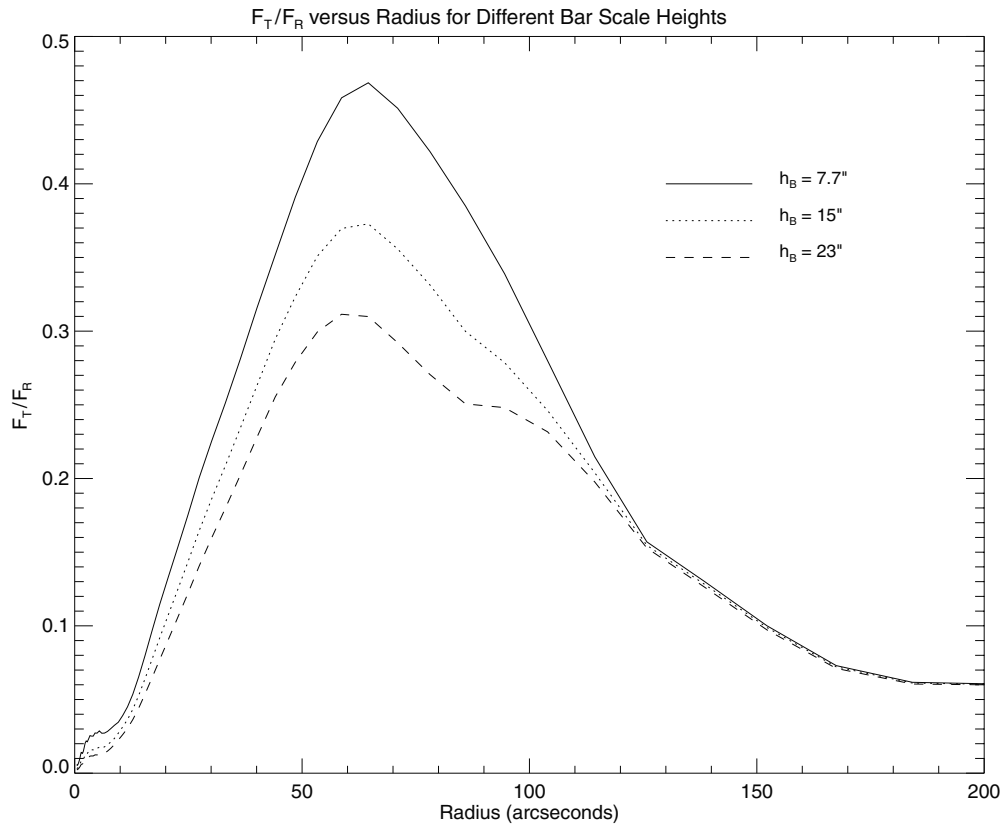
Figure 3. Plots of the tangential force amplitude (F_T) normalized by the axisymmetric disk force (F_R) for different bar scale heights (h_B). The bar scale heights range from one to three times the disk scale height of $7.7''$.

following the evolution of simulated exponential gaseous disks in order to describe the trends in spiral galaxy colors. Each M/L model corresponds to the various allowed parameters in the simulations. The Cole et al. (2000) model discussed by Bell & de Jong serves as a completely independent assessment of effects of galaxy evolution on these color trends.

The gravitational potentials were calculated for each of the seven M/L-corrected images by first using an iterative two-dimensional bulge-disk-bar decomposition described by Laurikainen et al. (2004). Upon application of the bulge-disk-bar decomposition it was found that the images that were M/L-corrected using the outflow and Cole et al. (2000) models did not converge through the iterative process and, therefore, were not used. The bulge component was then removed from the H-band light distribution and the disk was deprojected to a face-on orientation using a position angle of $21°$ and an inclination of $33°$ (Buta et al. 2001). The disk light distribution was approximated by an azimuthal Fourier decomposition at each radius and the disk gravity was calculated using the even components from $m = 0$ to $m = 8$, as was done by Rautiainen et al. (2005).

Other factors affect the morphology of a simulated galaxy besides the pattern speed. These include the impact frequency from the assumed cross section of the particles, initial particle distribution, and time when the features are examined. The amplitude of the bar is also an important factor affecting the modeled morphology. Separate exponential vertical distributions were, therefore, assumed for the disk and the bar. The bar component was isolated from the disk component upon determining the approximate length and, thereby, the orientation and ellipticity of the bar in the sky plane. The deprojected radius of the bar was already determined to be a maximum of approxi-

mately $115''$ by Block et al. (2004; see their Figure 1) through their Fourier bar-spiral separation technique on a deep K_s-band image. The orientation and ellipticity values of the bar at the given length in the sky plane were determined using ELLIPSE in IRAF.[3] A typical scale height of 1/6 the radial scale length (de Grijs 1998) was assumed for the disk component of the galaxy. Bureau et al. (2006) has advocated that the bar region of galaxies is subject to vertical thickening. Since the thickening factor is very uncertain, in Figure 3 we compare a range of thicknesses to Q_g, the maximum relative tangential perturbation F_T/F_R. This figure shows that a fairly large range in bar scale heights results in a rather small range of Q_g. We choose the scale height of the bar to be three times that of the disk, where Q_g is approximately 0.31. This corresponds to reducing the bar amplitude by a factor of 0.66, if the scale heights of the bar and disk are assumed to be equal (see Figures 9 and 10 for a display of the effects of bar amplitude variations). In comparison with the results of Buta et al. (2005; see their Figure 8), this value of Q_g means that approximately 70% of normal bright galaxies have bars weaker than that seen in NGC 1433. It has been argued that boxy- and peanut-shaped bulges are associated with relatively strong bars (Bureau et al. 2006) and that the ratio of bar length to thickness is 14 ± 4 for galaxies with these bulges (Lütticke et al. 2000). Therefore, we conclude that our bar scale height of $23''$ (corresponding to a bar length to thickness ratio of about 10) is not unreasonable for the assumed bar radius.

---

[3]　IRAF (Image Reduction and Analysis Facility) is distributed by the National Optical Astronomy Observatory, which is operated by the Association of Universities for Research in Astronomy, Inc., under cooperative agreement with the National Science Foundation.
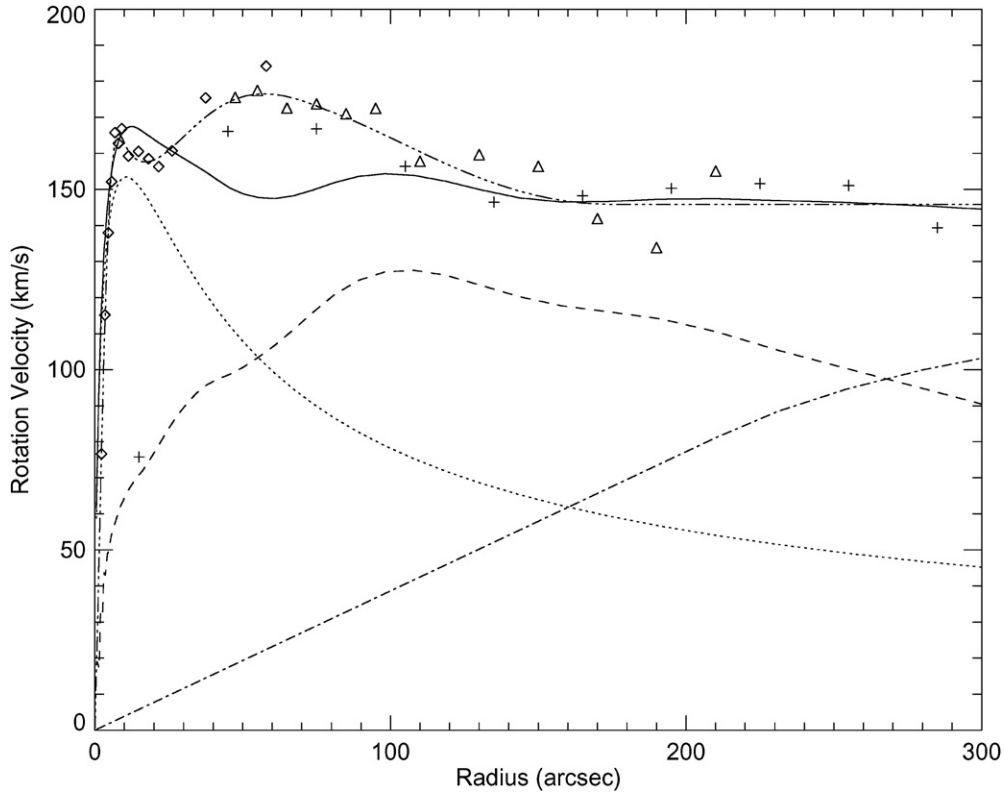
Figure 4. Plot of both the observed composite rotation curve (triple-dot-dashed line) and the simulation rotation curve (solid line) for NGC 1433. The composite rotation curve is from Buta et al. (2001), based on a polynomial fit to H I, Hα, and Mg I b velocity data (plus, triangle, and diamond symbols, respectively), corrected for an inclination of 33°. The points have typical statistical uncertainties of ±10–20 km s^{-1}, due to noncircular motions and an uncertain correction for asymmetric drift within 60″. Lines are also shown that indicate the azimuthally averaged velocity contributions of the bulge (dotted), disk (dashed), and halo (dot-dashed) used in the simulations. These lines were calculated from the mass model based on the formation epoch with bursts (Bell & de Jong 2001) M/L-corrected NIR image of the galaxy, an assumed disk vertical scale height of 7.7″, and a distance of 11.6 Mpc. The Persic halo component was modeled as an isothermal sphere with a core radius of 213″ and an asymptotic velocity at infinity of 127 km s^{-1}. The solid line is the sum of the component contributions or the total simulated rotation curve.
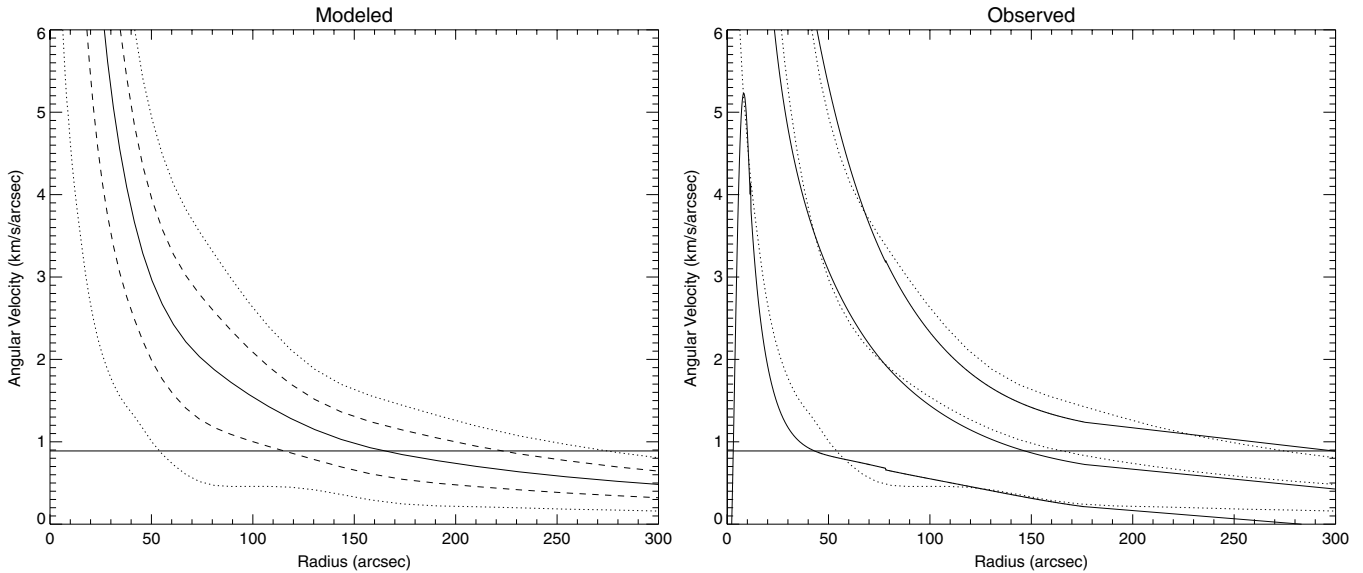

Figure 5. Lindblad precession frequency curves for NGC 1433. The horizontal line in both plots corresponds to the inclination-corrected Ω_p of 0.89 km s^{-1} arcsec^{-1} or 15.8 km s^{-1} kpc^{-1} with a galaxy distance of 11.6 Mpc. The left plot shows the frequency curves derived from the simulated rotation curve shown in Figure 2. The horizontal line intersects curves corresponding to, from smaller to larger radii, $\Omega - \kappa/2$, $\Omega - \kappa/4$, Ω, $\Omega + \kappa/4$, and $\Omega + \kappa/2$. Ω is the circular angular velocity and κ is the epicyclic frequency. The corotation radius is where $\Omega = \Omega_p$. The right plot displays the simulated $\Omega - \kappa/2$, Ω, and $\Omega + \kappa/2$ curves (dotted) with the corresponding curves derived from the observed composite rotation curve from Buta et al. (2001) overlaid (solid).

The gravitational potential of the bulge was also added to the disk potential under the assumption that the bulge mass is spherically distributed. Additionally, a dark halo component, based on the universal rotation curve of Persic et al. (1996) and scaled by approximately 1/3, was added to the galaxy potential so that the rotation amplitude at large radii ($r > 100″$) matched
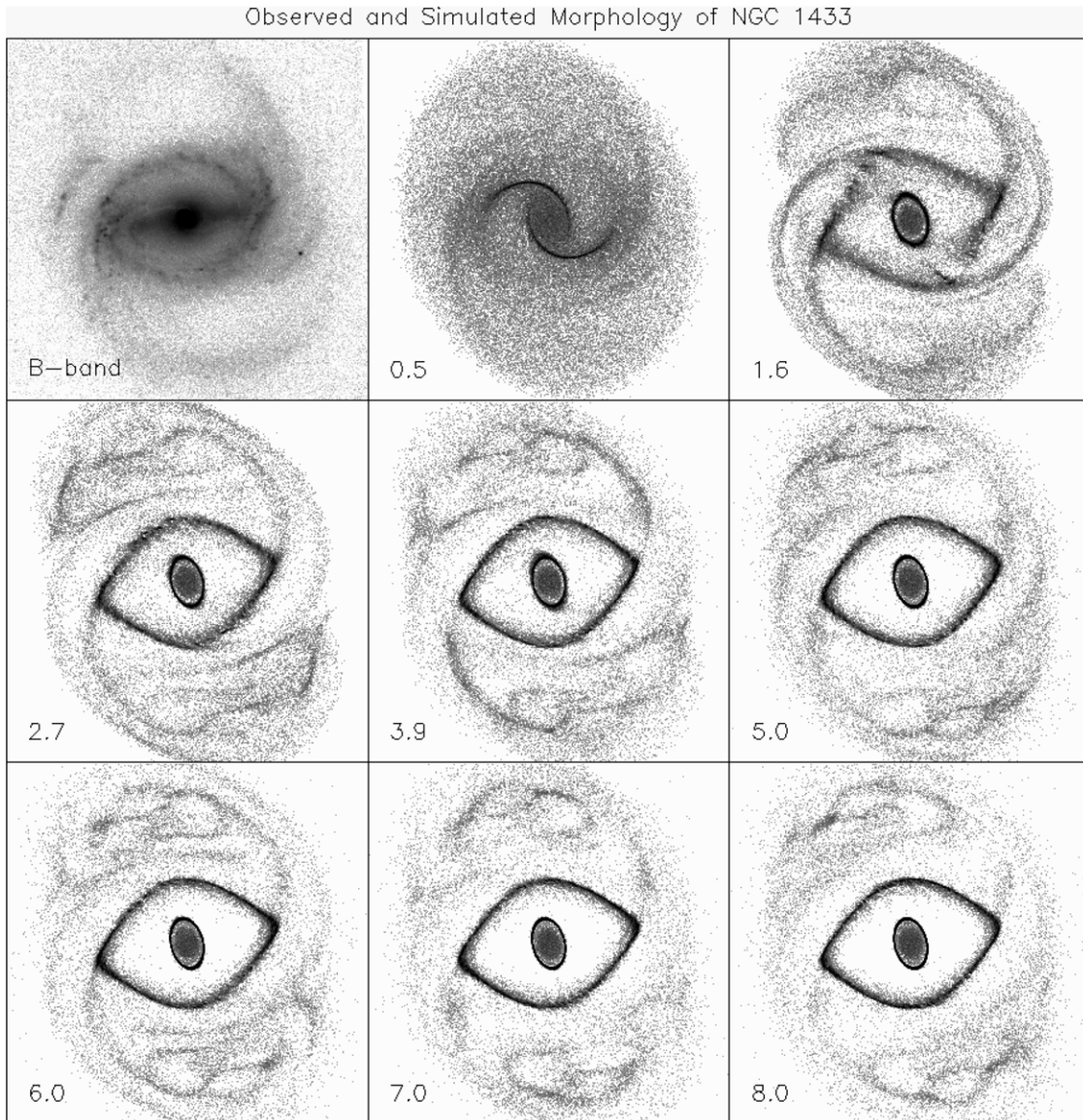
Figure 6. *B*-band image of NGC 1433 (upper left panel) showing the (R$'_1$)SB(rs)ab morphology. The remaining panels are gas simulations showing the sky-plane morphology at 0.5, 1.6, 2.8, 3.9, 5.0, 6.0, 7.0, and 8.0 bar rotations using a pattern speed of 0.89 km s^{-1} arcsec^{-1}. The simulated bar has a scale height three times larger than that of the disk. After a few bar rotations, the simulated and observed morphologies appear similar. Note the "plumes," or detached arm segments, to the upper left and lower right of the inner ring in the observed and simulated morphologies. All panels are 400 × 400 arcsec.

the composite rotation curve of Buta et al. (2001) as closely as possible (Figure 4). The effects of assuming a significantly more prominent halo can be estimated from the bar amplitude variation plots (see Figures 9 and 10). In Figure 4 there is a clear difference between the observed rotation curve, adopted by Buta et al. (2001), and that estimated from the azimuthally averaged mass model from approximately 30–100 arcsec. The observed rotation curve was derived from H i, Hα, and Mg i b data, where the H i rotation curve points were determined in Ryder et al. (1996) using the ROTCUR algorithm (based on the method discussed by Begeman 1989) within the Astronomical Image Processing System (AIPS). The Hα rotation points were derived from Fabry–Perot velocity field observations in Buta et al. (2001) using the Warner et al. (1973) method. The Mg i b major axis stellar velocity points were determined using the Fourier quotient (STSDAS routine FQUOT in IRAF) and cross-correlation methods (STSDAS routine XCOR; see Buta et al. 2001) and then applying the asymmetric drift correction

to make them comparable with gas velocity data. It should be noted that the observed inner rotation curve is uncertain due to noncircular motions and the uncertainties in the axisymmetric drift correction.

2.2. Simulations

The simulation code used to model NGC 1433 was written by H. Salo, the details of which can be found in Salo et al. (1999; see also Salo 1991 for the description of the treatment of inelastic collisions). The behavior of a two-dimensional disk of 100,000 inelastically colliding gas particles was simulated in the determined potential. The nonaxisymmetric part of the potential (i.e. the bar) was turned on gradually and reached full strength at one rotation. We assumed a single pattern speed for our models, that of the bar, and this was the main parameter that was varied. The morphology of the simulated gas distribution was compared to the morphology observed in the deep *B*-band
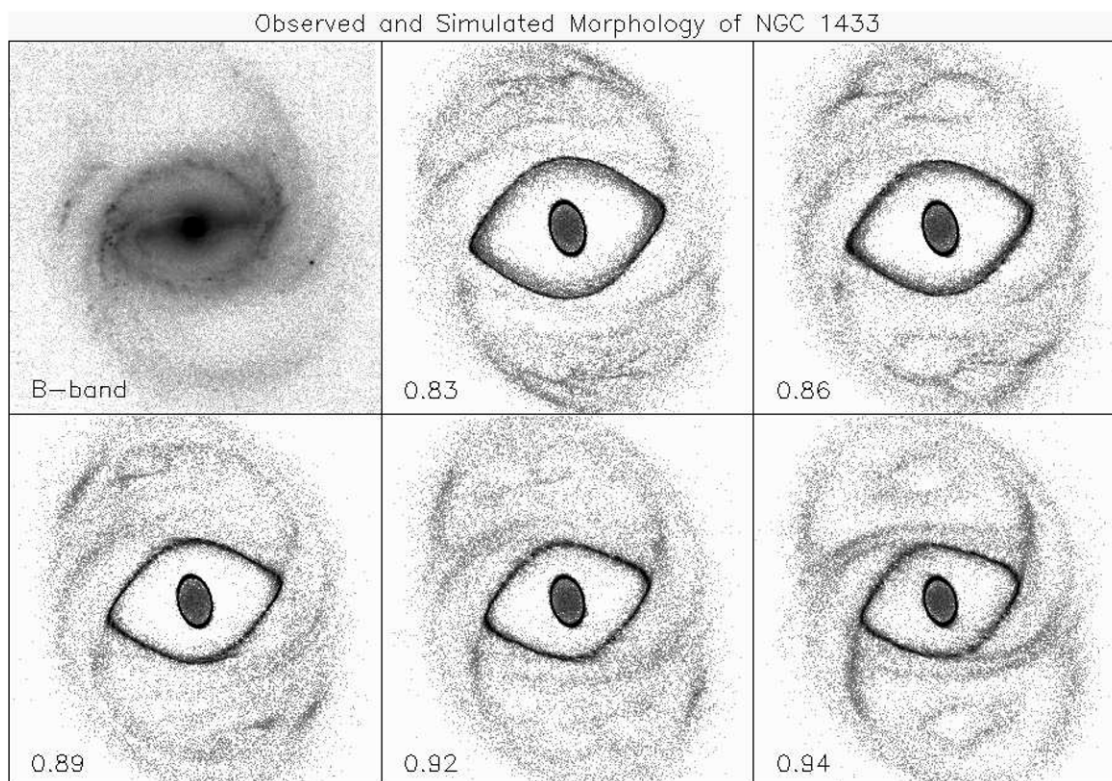
Figure 7. *B*-band image of NGC 1433 (upper left panel) showing the (R′₁)SB(rs)ab morphology. The remaining panels are gas simulations showing the morphology at 5.0 bar rotations with pattern speeds of 0.83, 0.86, 0.89, 0.92, and 0.94 km s⁻¹ arcsec⁻¹. The shape and position of the simulated plumes most closely resemble the *B*-band morphology with a pattern speed of 0.89 km s⁻¹ arcsec⁻¹ being used. Also note the decrease in the size of the inner ring with the increase in the pattern speed. All panels are 400 × 400 arcsec.

Table 1
Deprojected Feature Shape and Sizes[a]

Feature		a	b/a
(1)	(2)	(3)	(4)
Nuclear ring	Model	28.4 ± 2.2	0.76 ± 0.07
	Observation	8.9	0.9
Inner ring	Model	113 ± 8	0.56 ± 0.07
	Observation	107	0.63
Plumes	Model	167 ± 12	0.63 ± 0.09
	Observation	183	0.59
Outer pseudoring	Model	176 ± 15	0.98 ± 0.13
	Observation	190	0.89

Notes.
[a] Explanation of columns: (1) ring or feature; (2) data extracted from our best-fitting model at 5 bar rotation periods with $\Omega_p = 0.89$ km s⁻¹ arcsec⁻¹ and observations from Buta et al. (2001) where both assume a position angle of 21° and an inclination of 33°; (3) semimajor-axis radius in arcseconds; (4) axis ratio.

Table 2
Resonance Locations in NGC 1433

Resonance	Radius[a] (arcsec)	Radius[b] (arcsec)
Inner Lindblad resonance (ILR)	30.2[c]	54.0
Inner 4:1 ultraharmonic resonance (IUHR)	88.9	115.3
Corotation (CR)	120.9	165.1
Outer 4:1 ultraharmonic resonance (OUHR)	151.1	223.0
Outer Lindblad resonance (OLR)	192.0	274.5

Notes.
[a] Resonance radii from Table 5 of Buta et al. (2001) assuming a distance of 11.6 Mpc.
[b] Resonance radii from our best-fitting model, as seen in Figure 5.
[c] The OILR radius is given.

image of the galaxy. Since resonance rings generally form in the gas component, the observed *B*-band morphology is best suited for this purpose. The deep *B*-band image also lacks the gaps seen in the Hα data (Buta et al. 2001) and is of higher resolution than the existing H I data (Ryder et al. 1996). We specifically compared the visual size of the inner ring and outer pseudoring as well as the size and positioning of the plumes. The size of the nuclear ring is not easy to connect with the inner Lindblad

resonance (ILR) of the bar, therefore the nuclear ring region is not considered in the visual matching. Regarding the bar itself, dust lanes can be seen along it in optical images (Figure 1) and there is evidence for it in the H I intensity map of Ryder et al. (1996). CO emission was observed by Bajaja et al. (1995) and found to be peaked at the center of the galaxy and slightly elongated along the bar. Most of the CO intensity is found within approximately 30″ of the center, or less than half the bar radius. In the early phases of gas particle simulations, dust lanes are often seen but as the evolution proceeds the bar region becomes depleted of particles. In part, this is because the relative timescales of the inner and outer parts of the galaxy are not necessarily realistic. The impact frequency of the gas particles in the inner ring region is about 25 impacts/particle/bar rotation, whereas in the outer ring region it is about 2 impacts/particle/
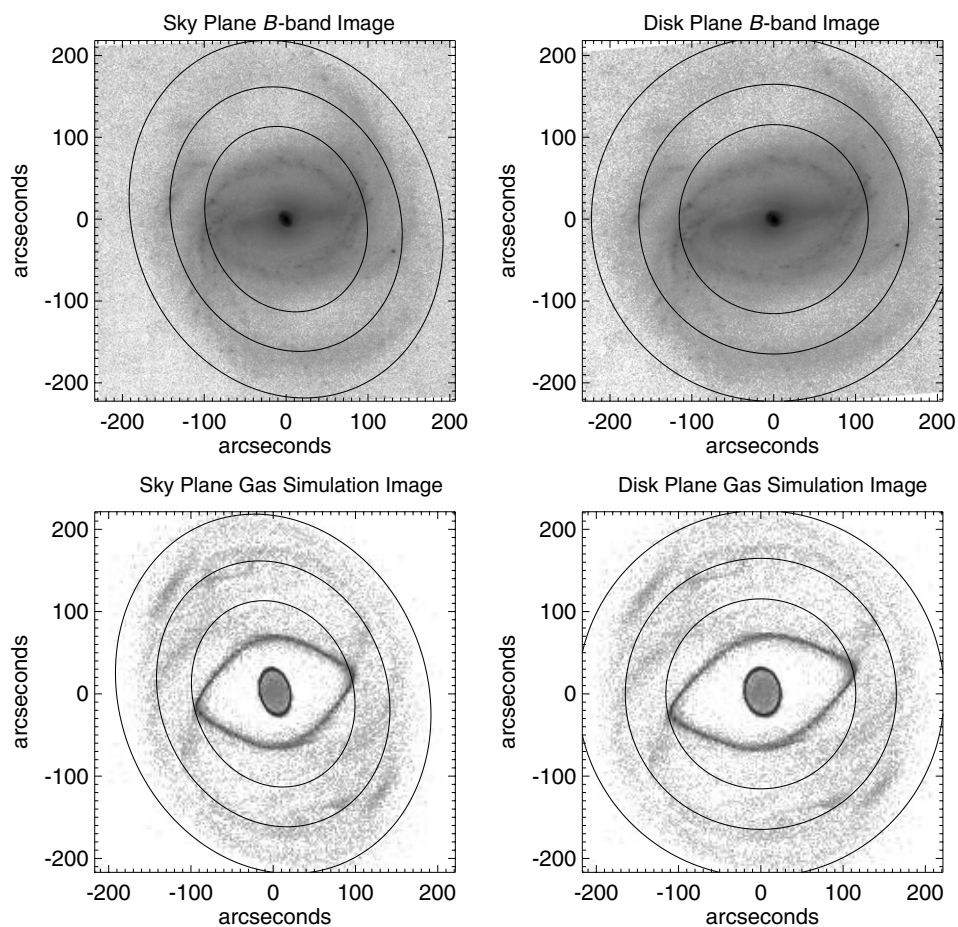
Sky Plane *B*-band Image   Disk Plane *B*-band Image

Sky Plane Gas Simulation Image   Disk Plane Gas Simulation Image

Figure 8. *B*-band disk- (upper left) and sky-plane (upper right) images of NGC 1433 along with disk- (lower left) and sky-plane (lower right) gas particle simulations shown at 5.0 bar rotations with a pattern speed of 0.89 km s^{-1} arcsec^{-1}. The overlaid ellipses are resonance locations derived from the shown gas particle simulations. The inner-most, middle, and outer-most ellipses correspond to the $\Omega - \kappa/4$, corotation, and $\Omega + \kappa/4$ resonances, respectively.
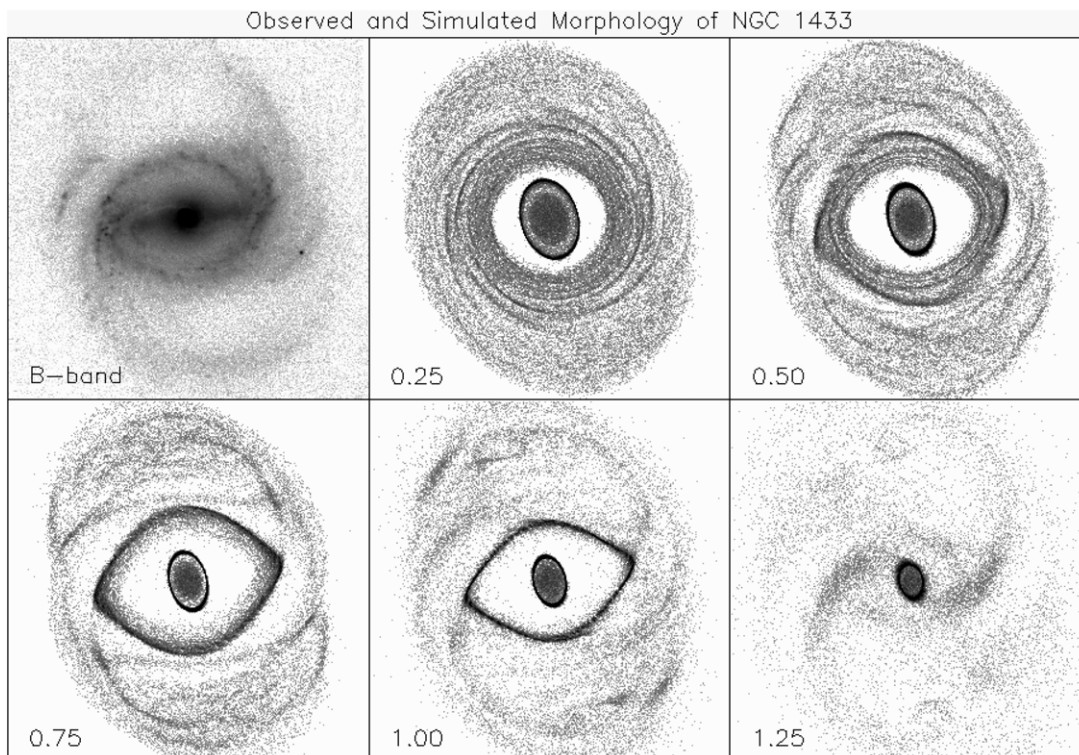
Observed and Simulated Morphology of NGC 1433

Figure 9. *B*-band image of NGC 1433 (upper left panel) showing the (R$_1'$)SB(rs)ab morphology. The remaining panels are gas simulations showing the morphology at 5.0 bar rotations with a pattern speed of 0.89 km s^{-1} arcsec^{-1} and bar amplitudes varying from 0.25 to 1.25. All panels are 400×400 arcsec.
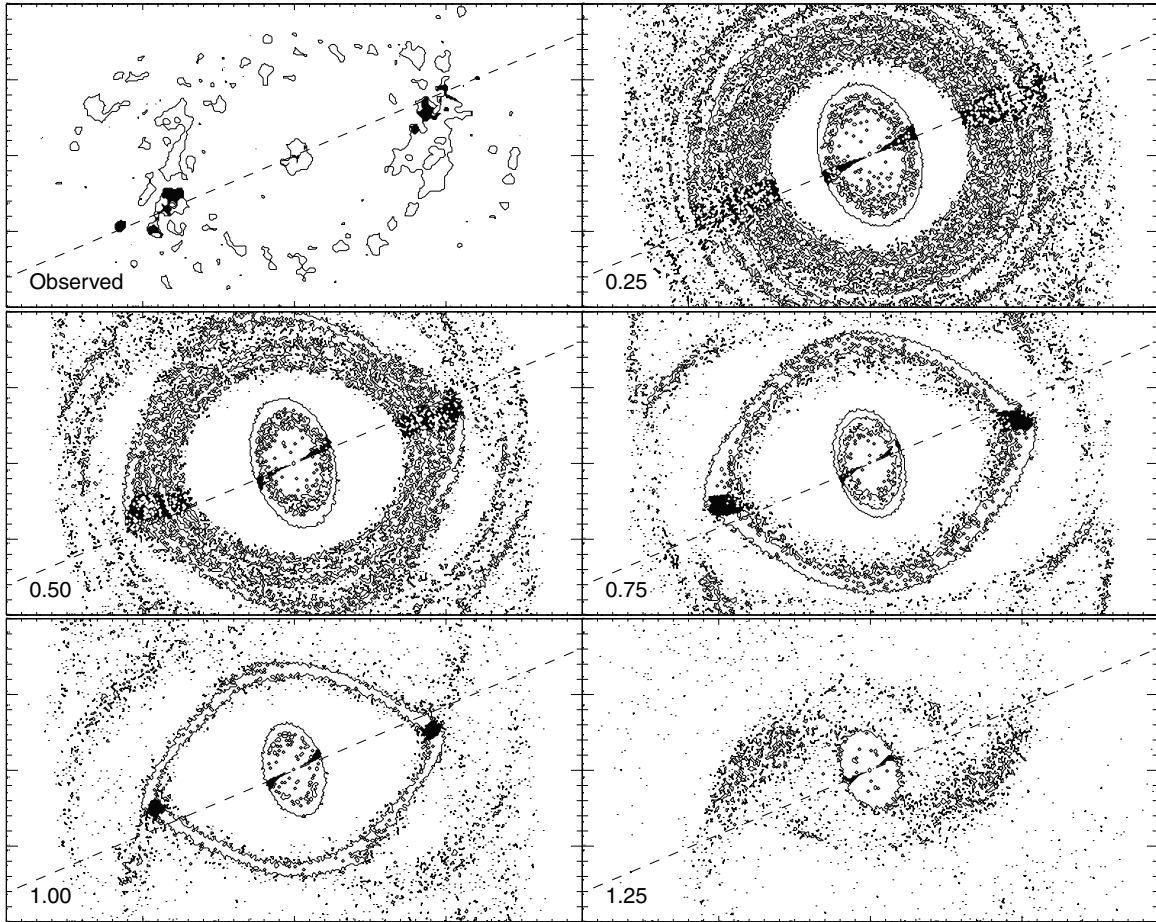
Figure 10. Zero-velocity regions (filled contours) from the observed and simulated data derived from velocities within ± 10 km s^{-1} of the systemic velocity. The upper left frame shows the Hα velocity field of NGC 1433 from Buta et al. (2001) while the remaining frames show the gas particle distribution at 5.0 bar rotations with an Ω_p of 0.89 km s^{-1} arcsec^{-1} and bar amplitude factors ranging from 0.25 to 1.25. The dashed line in the frames coincide with the galaxy's minor axis. All frames are 380×200 arcsec.

bar rotation. The timescale of evolution is rather arbitrary since it is determined by the assigned simulation parameters, mainly the radius of the gas particles, which have no direct physical correspondence to real gas. The gravitational potential is also static with respect to time which can cause the rigidly rotating bar to clean some regions of the disk with exaggerated efficiency. The additional caveat of the simulation code not taking gas recycling into account leads to a majority of the existing gas particles collecting at resonance locations. Overall though the morphology and size of the bar is a less accurate pattern speed estimator than the resonance ring and plume features.

2.3. Results and Discussion

In Figure 5 (left), we plot the Lindblad precession frequency curves derived from the simulated rotation curve estimated from the H-band image of the galaxy. These curves show how resonance locations vary with angular velocity in the linear (epicyclic) approximation. In this figure (right), we also see that the simulated outer Lindblad ($\Omega + \kappa/2$), corotation (Ω), and inner Lindblad ($\Omega - \kappa/2$) frequency curves appear similar to the same curves derived from the observed rotation curve data. A significant difference between the simulated and observed frequency curves is seen in the inner Lindblad curve. The curve derived from observational data is seen to reach a maximum of $\Omega - \kappa/2 \approx 5$ km s^{-1} arcsec^{-1}, whereas the simulated curve has no maximum. This is due to a subtle difference in the slopes

within a radius of $10''$, though the sparsity of observed data points leaves some ambiguity. The uncertainty of the inner rotation curve, due to corrections for asymmetric drift and noncircular motions, also propagates to the Lindblad frequency curves. A galaxy with a slowly rising rotation curve will have an inner Lindblad frequency curve that reaches a finite maximum (e.g., Yuan & Kuo 1997). This allows the possibility for the galaxy to host two ILRs, dubbed inner inner Lindblad resonance (IILR) and outer inner Lindblad resonance (OILR). If the bar rotates fast enough and the peak of the $\Omega - \kappa/2$ curve is low, it is also possible that there is no ILR. A fast rising rotation curve, on the other hand, will have an ILR curve with an infinite maximum and therefore only allow a single ILR. On the other hand, a secondary bar can also have considerable effect in this region.

In order to estimate Ω_p for NGC 1433, we would like to find the value that best matches the simulated and observed morphologies. For this purpose, we have the inner ring, the plumes, and the outer pseudoring as features that a good simulation ought to match. The nuclear ring, however, is not considered in the matching since its size is much more sensitive to the strength of the perturbation and the method of the gas treatment. Good agreement between the size of the inner and outer rings, as well as the position and orientation of the plumes, is obtained at 5 bar rotation periods with a pattern speed of 0.89 km s^{-1} arcsec^{-1}, or 15.8 km s^{-1} kpc^{-1} with an

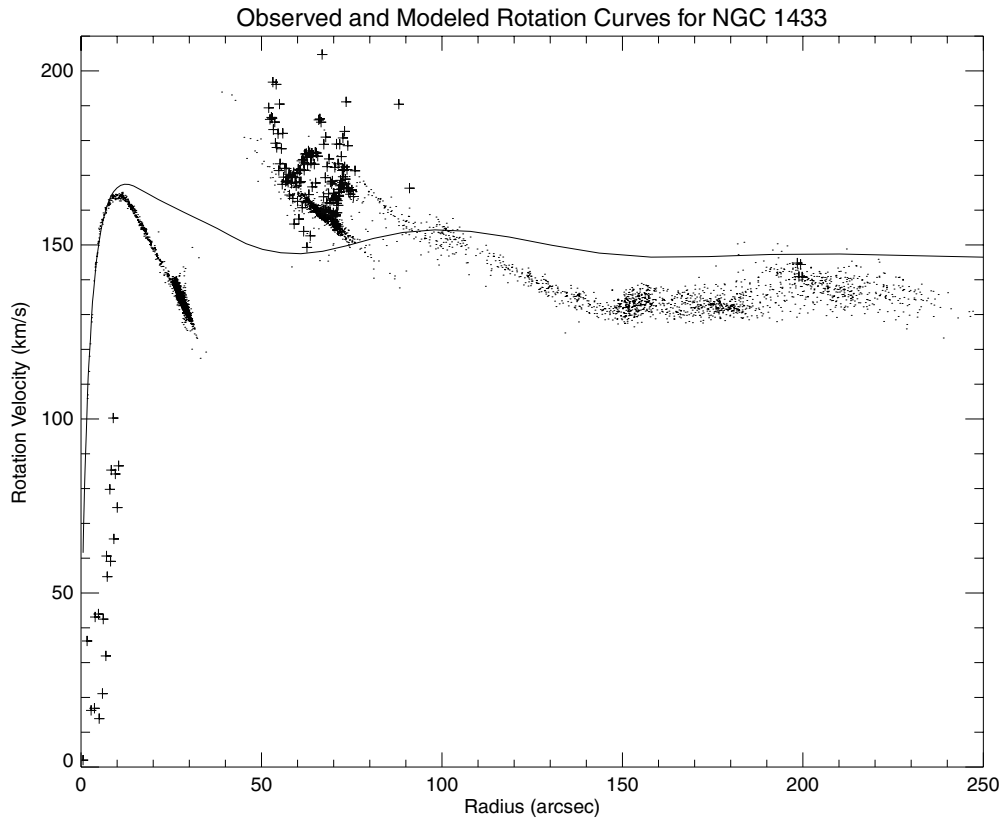Observed and Modeled Rotation Curves for NGC 1433

Figure 11. Plot of the observed (plus symbols) and modeled (points) major axis velocity profiles for NGC 1433, as well as the azimuthally averaged total velocity contribution calculated from the mass model (line) discussed in Figure 4. The major axis velocity profiles are derived from the observed Hα velocity field (from Buta et al. 2001) and the modeled gas particle distribution at 5 bar rotations with an Ω_p of 0.89 km s^{-1} arcsec^{-1}. The velocity profile data were extracted from within 5° of the major axis position angle of 21° and corrected for an inclination of 33°. The deviation between the model and the observed gas velocities for radii less than 20″ is due in part to noncircular motions, manifested as a 9° counterclockwise offset between the kinematic major axis of the inner velocity field in Figure 6 of Buta et al. (2001) and the overall position angle. The deviation is also due to the model which we have shown does not describe the inner regions reliably owing to our assumption of a single pattern speed and other model details.

assumed distance of 11.6 Mpc (Block et al. 2004), and using the formation epoch M/L model with bursts from Bell & de Jong (2001; see Table 1 and Figure 6). The gravitational potentials derived from the other M/L models did not cause the simulated morphology of the galaxy to differ significantly. The plumes found in the simulations are transient features that are seen to dissipate after about 5 bar rotations. They begin as complete spiral arms emerging from a very boxy model inner ring and evolve to detached segments. A variation in the pattern speed of approximately ±5–10% also prevents the plumes from taking a shape similar to what is seen in the B-band (Figure 7). This is also true when the bar scale height is reduced. The inner and outer ring sizes were only dependent on the bar pattern speed. The simulated inner ring has a similar size and elongation to the observed galaxy, but appears more diamond shaped. The shape of the inner ring can sensitively depend on the orbit families in this region, where a rather small change in parameters (e.g., Ω_p or bar amplitude) could lead to a large change in morphology. Since the assumed single bar pattern speed gives both the inner ring and the structure beyond it, there is no obvious need for a possible outer, slower spiral mode obtained in other barred spiral simulations (e.g., Rautiainen & Salo 1999). It should be noted that all the simulation timescales are very uncertain. For example, the gas particle parameters, the rigidity of the gravitational potential, and the lack of gas recycling in the system all affect the dynamical timescale of the simulation.

Examining the morphology of the galaxy, we find that the observed inner ring corresponds to the location of the simulated

inner 4:1 resonance ($\Omega_p = \Omega - \kappa/4$) and the outer pseudoring lies between the corotation resonance and outer 4:1 resonance ($\Omega_p = \Omega + \kappa/4$) (Figure 8). The plumes and the outer pseudoring lie between the inner and outer ($\Omega + \kappa/4$) 4:1 resonances, similar to what was determined for ESO 566−24 (Rautiainen et al. 2004). An outer ring was also shown to occasionally form within the outer 4:1 resonance, instead of near the outer Lindblad resonance (OLR), in an N-body model produced by Rautiainen & Salo (2000). This suggests that some outer pseudorings that show the R$_1'$ morphology (Buta & Crocker 1991) are not actually OLR features. This was already hinted at observationally by ESO 566−24, where two of the four outer arms were noted to form an R$_1'$ morphology by Buta et al. (1998). In this galaxy, a clear detached outer ring that encircles the $m = 4$ pattern could trace the actual location of the OLR.

These results may be compared with the precession frequency analysis made by Buta et al. (2001, their Figure 14), who used preliminary numerical simulations from Buta & Combes (2000) to set the pattern speed at 1.3 km s^{-1} arcsec^{-1}. These simulations did not reproduce the plumes of NGC 1433, and the derived pattern speed placed the OLR closer to the radius of the outer pseudoring than do our present simulations. In Table 2, we summarize the resonance radii derived by both Buta et al. (2001) and our best model. Our model predicts that the OLR is at a radius of about 1.4 times larger than the observed major axis radius of the outer pseudoring. The radial distribution of the azimuthally averaged H I surface density published by Ryder et al. (1996, their Figure 6) shows that there is very little gas in
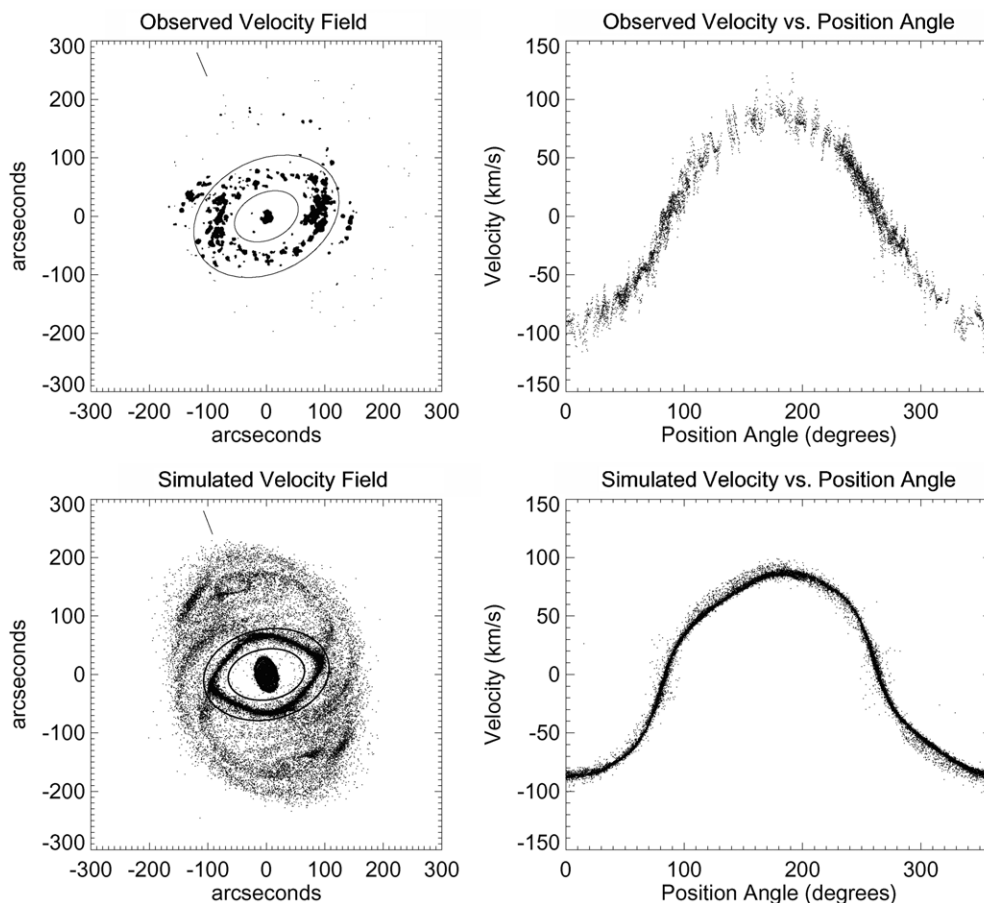
Figure 12. Line-of-sight velocities along the inner ring of NGC 1433. The leftmost plots show the annuli where the inner ring velocity data were extracted from the observed Hα velocity field from Buta et al. (2001) (upper) and the simulated gas particle distribution at 5.0 bar rotations with an Ω_p of 0.89 km s^{-1} arcsec^{-1}. The angled line near the top of the frames coincides with the line-of-nodes of the galaxy. The rightmost plots show the line-of-sight velocity versus the position angle relative to the line-of-nodes along the ring from the observed (upper) and simulated (lower) data. There is a clear asymmetry in both the observed and simulated radial velocity data along the inner ring.

the OLR region predicted by our new simulations. This may explain why no features associated with this resonance are observed in NGC 1433.

An obvious difference between the simulated and observed morphologies is the size of the nuclear ring. The nuclear ring seen in the simulations is much larger than what is observed in the actual galaxy. According to Buta & Combes (1996), nuclear rings tend to form near the IILR if it exists. By plotting our value of Ω_p over the Lindblad precession frequency curves in Figure 5, we are able to predict where resonances occur by determining the radius at which the Ω_p line crosses a corresponding frequency curve. For the observed inner Lindblad frequency curve, the smallest intersection radius is near 3″. In Table 1 of Buta et al. (2001), the semimajor axis radius of the nuclear ring is given as 0.5 kpc at a distance of 11.6 Mpc, or 8.9″, which is about three times the estimated linear resonance radius. In the case of the simulation, the fast rising rotation curve forces the nuclear ring to form near the single ILR which corresponds to the OILR derived from the observed rotation curve. The presence of a secondary bar with a different pattern speed is a further complication. The observed nuclear ring can be an example of loops which were introduced by Maciejewski & Sparke (2000) in orbit analysis in double barred potentials and simulated by Rautiainen et al. (2002). In principle, a stronger bar perturbation, due to the bar being less vertically extended for example, would shift the nuclear ring inward from the linear

ILR distance (see, e.g., Salo et al. 1999). However, decreasing the scale height of the bar did not have a significant effect on the size of the nuclear ring. In contrast, Regan & Teuben (2003) have stated that the ILR does not exist for a galaxy with a strong bar, like NGC 1433, since there is no resonance with the rotating potential at that radius. Instead, they showed through their hydrodynamical models that nuclear rings result from the interaction of gas on x_1-like and x_2-like streamlines. This suite of uncertainties in the central region of NGC 1433 indicates that the observed nuclear ring does not serve as an accurate indicator of Ω_p.

In an effort to examine the expected deviations from the linear epicyclic approximation caused by a strong bar, we have produced models of different bar amplitudes (e.g., the nonaxisymmetric Fourier components of the potential were multiplied by a factor while the axisymmetric component was kept intact). In Figure 9, we compare the observed gas morphology to models at 5 bar rotations with Ω_p equal to 0.89 km s^{-1} arcsec^{-1} and with bar amplitudes varied by a factor of 0.25–1.25. As mentioned earlier, these models also serve to describe the possible effects of uncertainties in factors such as bar height or the contribution from the halo. The results are similar to those found when the bar amplitude of IC 4214 was varied by Salo et al. (1999). As the amplitude is increased from a factor of 0.25–1.00, the inner ring becomes well defined and increases in ellipticity. The ring nearly vanishes when
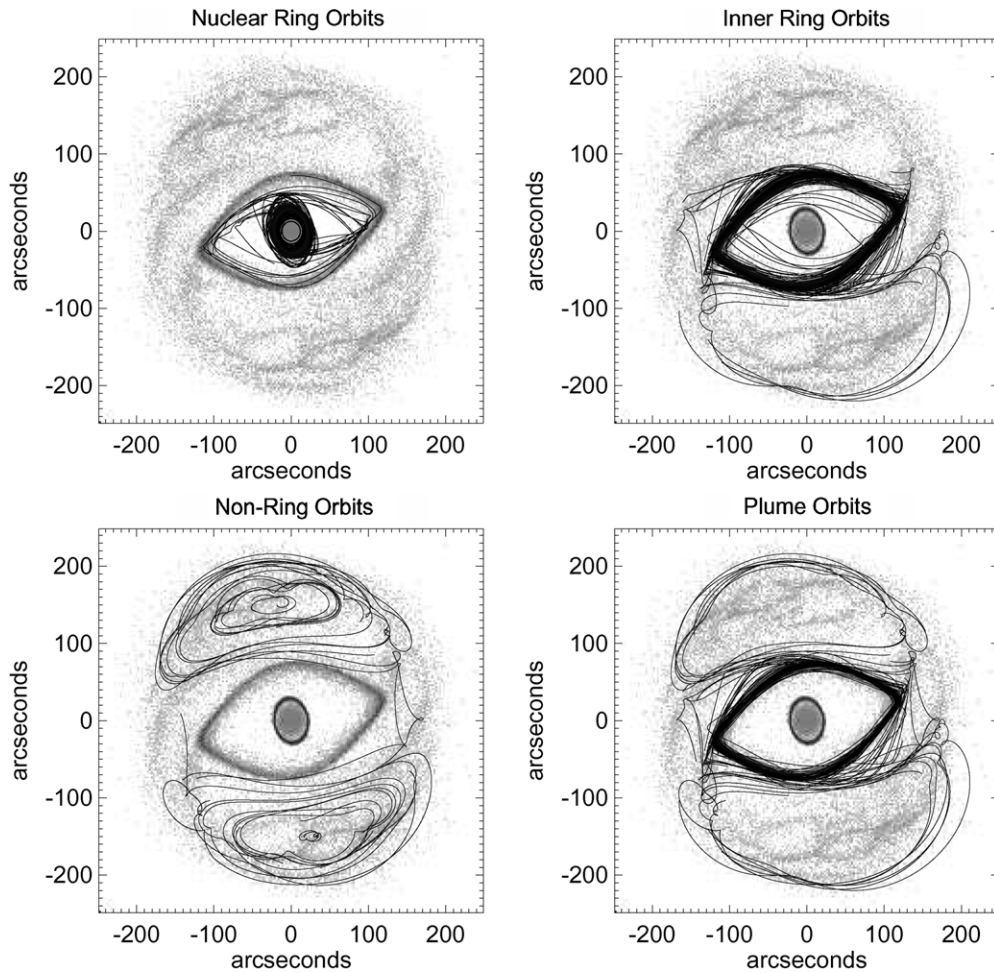
Figure 13. Plots of selected gas particle orbits from 1.0 to 5.0 bar rotations overlaid on the simulated gas particle distribution at 5.0 bar rotations with $\Omega_p = 0.89$ km s^{-1} arcsec^{-1}. The upper left and upper right plots display the orbits that conclude in the nuclear and inner ring of the simulation, respectively. The lower left plot displays orbits trapped near the L_4 and L_5 Lagrangian points. The lower right plot displays orbits that pass through the regions of the plumes. Most of these gas particles were found to conclude their orbits in the inner ring. All of the plots are in the disk plane of the simulation and the orbits are shown in the rotating frame.

the amplitude is increased by a factor of 1.25. The resultant morphology from varying the amplitude indicates that the shape of the observed inner ring may be due to a somewhat weaker perturbation than assumed in the nominal model. Also, as the bar amplitude of the model is increased, the size of the nuclear ring decreases.

In Figure 10, we compare the observed and simulated kinematics of the galaxy by examining the zero-velocity contour, which is sensitive to bar-induced radial velocities. We compare the Hα Fabry–Perot velocity field found in Buta et al. (2001) with the simulated gas velocity fields derived from various bar amplitudes. Agreements between the observed and simulated kinematics of the galaxy support our estimate of Ω_p with a bar amplitude factor close to 1. Although the observed velocity field is not as rich with data as the simulated velocity field, the zero-velocity contours show similar characteristics within 100″ from the galaxy center. A comparison of the observed and modeled major axis velocity profiles (Figure 11), sensitive to bar-induced tangential velocity increments, reveals a similar behavior between approximately 50″ and 80″. A deviation is seen between the azimuthally averaged total velocity contribution calculated from the mass model and the major axis velocity profile near 30″ due to the large nuclear ring in the model. Particles in this ring, near the major axis, are close to their apocenter

and are therefore moving slower than their average orbital velocity. At larger radii, the modeled major axis velocity profile is approximately 15 km s^{-1} less than the azimuthally averaged total velocity contribution used in the simulations. In principle, the match in this region could be easily improved by assuming a somewhat larger halo contribution. This would also reduce the relative bar perturbation.

Also, the asymmetry seen in the simulated radial velocity of the gas found in the inner ring of the galaxy is similar to what is observed (Figure 12). The upper right panel of this figure shows the velocity–position angle diagram for points confined between the two ellipses shown in the upper left panel. The observed velocity–position angle diagram shows a subtle asymmetry that was also detected by Buta (1986) and interpreted in terms of ring material moving along an oval bar orbit. The lower right panel of Figure 12 shows the same diagram for the simulated inner ring, showing a similar asymmetry. The main difference is that the simulated curve is steeper near position angles of 100° and 280° owing to the more pointy oval shape of the simulated inner ring. By fitting a simple orbit model to the observed velocity–position angle diagram, Buta (1986) estimated a pattern speed of 1.55 ± 0.4 km s^{-1} arcsec^{-1}. If the bar were exactly perpendicular or parallel to the line-of-nodes, this asymmetry would not be seen, as in the case of NGC 3351 (Buta 1988).

Because of the versatility of the modeling process, we are able to track a number of individual gas particles for the duration of a simulation. In Figure 13, we show the paths of selected gas particles in the rotating frame of the simulated galaxy from 1.0 (when the bar has reached full strength) to 5.0 bar rotations where $\Omega_p = 0.89$ km s^{-1} arcsec^{-1}. We find that the nuclear ring is partially made up of gas particles that originate from near the final location of the inner ring. The inner ring includes some particles drawn from outside the final inner ring location. The transient plumes seen in the simulations appear to be due to both gas trapped in the outer banana orbits and traveling from theses orbits inward toward the inner ring.

Determining a value for Ω_p also allows us to estimate $\mathcal{R} \equiv R_{\rm CR}/R_B$ where $R_{\rm CR}$ is the corotation radius of the galaxy and R_B is the bar semimajor axis length. If this distance-independent ratio is between 1.0 and 1.4, a bar is said to be "fast," while if greater than 1.4, a bar is said to be "slow." Contopoulos (1980) concluded that self-consistent bars cannot exist when $\mathcal{R} < 1.0$, although Zhang & Buta (2007) have argued to the contrary. Debattista & Sellwood (2000) contend that fast bars exist in halos with a low central concentration since the bar rotation rate would rapidly decrease due to dynamical friction with the halo. Certain galaxy models from Athanassoula (2003) also show this correlation between fast bars and halos of low central concentration. The value of $R_{\rm CR}$ is found by determining the radius at which $\Omega_p = \Omega$ in the simulation. For our Ω_p value of 0.89 ± 0.06 km s^{-1} arcsec^{-1}, the average $R_{\rm CR}$ value is $162.5 \pm 11.9''$ (see Figure 5).

The deprojected value of R_B was estimated to be $82''$ (4.6 kpc) by Buta et al. (2001). With our average value of $R_{\rm CR}$, this would imply an upper limit of $\mathcal{R} = 2.0$. This is because $R_B = 82''$ refers to the apparent sharp ends of the bar and may not be the best estimate of the actual bar radius. Based on a bar-spiral Fourier separation analysis, Figure 1 of Block et al. (2004) suggests that the bar extends to a maximum radius of $115 \pm 5''$. This value implies that the lower limit of $\mathcal{R}$ is 1.4 ± 0.1. An average of these R_B values ($98.5''$) yields $\mathcal{R} = 1.7 \pm 0.3$, with the error largely due to the ambiguity in the bar length. In any case, NGC 1433 may be in the "slow bar" domain of Debattista & Sellwood (2000). Most previous direct measurements of bar pattern speeds in early-type galaxies have not found slow bars (e.g., Corsini et al. 2003, 2007; Debattista & Williams 2004; Aguerri et al. 2003).

3. CONCLUSIONS

Using NIR images to trace the stellar disk potential, we have located resonances in NGC 1433, an exceptional barred spiral galaxy having strong morphological features. The numerical simulation method of Salo et al. (1999; see also Rautiainen et al. 2005) was used to interpret the structure of the galaxy by matching a cloud-particle model to the observed morphology. The results are consistent with previous studies such as Schwarz (1984), Byrd et al. (1994), Rautiainen & Salo (2000), and Rautiainen et al. (2004). Our best simulation model provides an interpretation of NGC 1433 which places corotation at 1.7 times the average estimated bar radius of about $100''$. This model also places the inner 4:1 resonance near the cuspy ends of the highly elongated inner ring and just outside the ends of the bar.

The plumes and the two outer arms forming the R$'_1$ outer pseudoring appear completely confined between the inner and outer 4:1 resonances, very similar to what Rautiainen et al. (2004) found for the symmetric $m = 4$ barred spiral ESO 566−24. The plumes, which are like detached spiral segments,

appear to be evolved versions of the two extra "side arms" of ESO 566−24 that wrap around the bar ends.

The predicted location of the OLR in NGC 1433 is well outside the outer pseudoring in a region where there is little H I gas (Ryder et al. 1996). Thus, NGC 1433 presents an example of an "OLR subclass" outer pseudoring (Buta & Crocker 1991; Buta et al. 2007) that is *not* associated with the OLR.

REFERENCES

Aguerri, J. A. L., Debattista, V. P., & Corsini, E. M. 2003, MNRAS, 338, 465
Athanassoula, E. 2003, MNRAS, 341, 1179
Bajaja, E., Wielebinski, R., Reuter, H.-P., Harnett, J. I., & Hummel, E. 1995, A&AS, 114, 147
Begeman, K. G. 1989, A&A, 223, 47
Bell, E. F., & de Jong, R. S. 2001, ApJ, 550, 212
Block, D. L., Buta, R., Knapen, J. H., Elmegreen, D. M., Elmegreen, B. G., & Puerari, I. 2004, AJ, 128, 183
Bureau, M., Aronica, G., Athanassoula, E., Dettmar, R.-J., Bosma, A., & Freeman, K. C. 2006, MNRAS, 370, 753
Buta, R. 1984, PASA, 5, 472
Buta, R. 1986, ApJS, 61, 631
Buta, R. 1988, ApJS, 66, 233
Buta, R., Alpert, A., Cobb, M. L., Crocker, D. A., & Purcell, G. B. 1998, AJ, 116, 1142
Buta, R., & Combes, F. 1996, Fund. Cosmic Phys., 17, 95
Buta, R., & Combes, F. 2000, ASP Conf. Ser., 197, 11
Buta, R. J., Corwin, H. G., & Odewahn, S. C. 2007, The de Vaucouleurs Atlas of Galaxies (Cambridge: Cambridge Univ. Press) (BCO)
Buta, R., & Crocker, D. A. 1991, AJ, 102, 1715
Buta, R., Ryder, S. D., Madsen, G. J., Wesson, K., Crocker, D. A., & Combes, F. 2001, AJ, 121, 225
Buta, R., Vasylyev, S., Salo, H., & Laurikainen, E. 2005, AJ, 130, 506
Byrd, G., Rautiainen, P., Salo, H., Buta, R., & Crocker, D. A. 1994, AJ, 108, 476
Cole, S., Lacey, C. G., Baugh, C. M., & Frenk, C. S. 2000, MNRAS, 319, 168
Contopoulos, G. 1980, A&A, 81, 198
Corsini, E. M., Aguerri, J. A. L., Debattista, V. P., Pizzella, A., Barazza, F. D., & Jerjen, H. 2007, ApJ, 659, 121L
Corsini, E. M., Debattista, V. P., & Aguerri, J. A. L. 2003, ApJ, 599, 29L
de Grijs, R. 1998, MNRAS, 299, 595
Debattista, V. P., & Sellwood, J. A. 2000, ApJ, 543, 704
Debattista, V. P., & Williams, T. B. 2004, ApJ, 605, 714
Kalnajs, A. 1991, in Dynamics of Disk Galaxies, ed. B. Sundelius (Göteborg: Göteborg Univ.), 323
Laurikainen, E., & Salo, H. 2002, MNRAS, 337, 1118
Laurikainen, E., Salo, H., Buta, R., & Vasylyev, S. 2004, MNRAS, 355, 1251L
Lütticke, R., Dettmar, R.-J., & Pohlen, M. 2000, A&A, 362, 435
Maciejewski, W., & Sparke, L. S. 2000, MNRAS, 313, 745
Persic, M., Salucci, P., & Stel, F. 1996, MNRAS, 281, 27
Quillen, A. C., Frogel, J. A., & Gonzalez, R. A. 1994, ApJ, 437, 162
Rautiainen, P., & Salo, H. 1999, A&A, 348, 737
Rautiainen, P., & Salo, H. 2000, A&A, 362, 465
Rautiainen, P., Salo, H., & Buta, R. 2004, MNRAS, 349, 933
Rautiainen, P., Salo, H., & Laurikainen, E. 2002, MNRAS, 337, 1233
Rautiainen, P., Salo, H., & Laurikainen, E. 2005, ApJ, 631, L129
Regan, M. W., & Teuben, P. 2003, ApJ, 582, 723
Ryder, S. D., Buta, R. J., Toledo, H., Shukla, H., Staveley-Smith, L., & Walsh, W. 1996, ApJ, 460, 665
Salo, H. 1991, A&A, 243, 118
Salo, H., Laurikainen, E., & Buta, R. 2004, ASSL, 319, 673
Salo, H., Rautiainen, P., Buta, R., Purcell, G. B., Cobb, M. L., Crocker, D. A., & Laurikainen, E. 1999, AJ, 117, 792
Schwarz, M. P. 1981, ApJ, 247, 77
Schwarz, M. P. 1984, MNRAS, 209, 93
Warner, P. J., Wright, M. C. H., & Baldwin, J. E. 1973, MNRAS, 163, 163
Yuan, C., & Kuo, C. 1997, ApJ, 486, 750
Zhang, X., & Buta, R. 2007, AJ, 133, 2584